Isochronous lattice design with time-of-flight fluctuation reaching subattoseconds based on high-order achromat

Zhilong Pan,[*,†] Jingyuan Zhao,[*] and Chuanxiang Tang
Department of Engineering Physics, Tsinghua University, Beijing 100084, China
and Key Laboratory of Particle and Radiation Imaging, Tsinghua University, Beijing, China

Xiujie Deng and Alexander Wu Chao
Institute for Advanced Study, Tsinghua University, Beijing, China

(Received 22 August 2025; accepted 3 December 2025; published 30 December 2025)

The fluctuation in electron time of flight during lattice transport is crucial for various applications, such as ultrafast electron diffraction, optical stochastic cooling in storage rings, and sustaining steady-state microbunching in storage rings. A major issue impacting the time-of-flight fluctuation of the electron beam during transport is the lattice's nonlinear effects. In this study, we introduce a design concept aimed at reducing the electron beam's time-of-flight fluctuation in an isochronous lattice up to the subattosecond level. This approach employs a high-order achromat lattice that effectively eliminates time-of-flight contributions arising from low-order nonlinearities. We also present an optimized design example based on this concept, achieving approximately 0.3 attoseconds root-mean-square time-of-flight fluctuation (equivalent to 0.1 nm) with specific beam emittance values of $\epsilon_x \sim 1$ nm, $\epsilon_y \sim 1$ nm, and $\sigma_\delta \sim 1 \times 10^{-3}$.

DOI: 10.1103/3v8n-84fr

I. INTRODUCTION

During beam transport, fluctuations in the beam's time of flight are critical factors that impact its use in various applications. These fluctuations arise from multiple sources, including the lattice design and the stability of the power supplies for magnets and rf systems. In ultrafast electron diffraction, one of the key limitations on resolution is the time-of-flight variation of the electron beam. As reported by Qi *et al.* [1], achieving a bunch length of 29 fs and an arrival time jitter of 22 fs allows for a resolution of 50 fs in MeV ultrafast electron diffraction. Although lattice nonlinearity does not appear to be a major contributor to arrival time jitter in Qi's study, it may become a more significant issue as technology progresses. Meanwhile, the isochronous lattice is becoming increasingly important because of the requirement for precise control of longitudinal dynamics in emerging storage ring concepts, such as optical stochastic cooling (OSC) [2–4] and steady-state microbunching (SSMB) [5–7]. For example, Zholents [4] mentioned that when designing the OSC cooling system, the time-of-flight variation caused by lattice nonlinearities should be limited to no more than 1.7 attoseconds (roughly 0.5 nm). In the SSMB scheme, the acceptable time-of-flight fluctuation between the upstream and downstream modulators in the lattice is approximately 0.3 nm (around 1 attosecond) to attain a high average radiation power of 1 kW at extreme ultraviolet wavelengths [8]. Additionally, in several high-power storage ring light source designs that incorporate longitudinal dynamics control [9–11], the fluctuation in the electron beam's time of flight between modulation and demodulation plays a crucial role in radiation power. In these light source schemes, time-of-flight variations of electron beam between modulation and demodulation cause imperfect cancellation, resulting in substantial emittance growth of the electron beam each time it passes through this lattice section. To mitigate this emittance growth, the authors suggested alternative approaches such as employing a bypass line [9,10] or triggering the modulation only once every few hundred turns [11], leading to a decrease in the radiation repetition rate by several hundred fold.

There is a high demand for an isochronous lattice design capable of achieving time-of-flight fluctuations on the order of attoseconds for these applications. We would like to clarify that our definition of time-of-flight fluctuation refers to the variance of $\Delta t = t_f - t_i$, where t_f is the final time coordinate of an electron traversing the lattice, and t_i is the initial time coordinate of the same electron. Previously, the design of isochronous storage rings primarily focused on implementing the low-alpha scheme [12–15] to achieve relatively short electron bunch lengths. High-order transverse-longitudinal

[*]These authors contributed equally to this work.
[†]Contact author: panzl@mail.tsinghua.edu.cn

Published by the American Physical Society under the terms of the Creative Commons Attribution 4.0 International license. Further distribution of this work must maintain attribution to the author(s) and the published article's title, journal citation, and DOI.

coupling was not a major concern, as its effects were considered negligible compared to the bunch length itself. Additionally, numerous studies have explored high-order achromat (HOA) lattice designs [16–23], which are beneficial for optimizing nonlinear dynamics in storage rings. However, to date, there has been no systematic investigation into optimizing time-of-flight fluctuations of electron bunches arising from the lattice. This paper aims to present a method based on HOA to minimize these time-of-flight fluctuations down to the attosecond level. This paper is structured as follows. Section II outlines the problem we aim to address and discusses the suitability of the HOA scheme for this purpose. Section III provides an optimized design example of a lattice based on HOA concept. In Sec. IV, we preliminarily discuss the impact of misalignment error of quadrupoles on the time-of-flight fluctuations. Lastly, we conclude our work in Sec. V.

II. PROBLEM DEFINITION

We will begin with the SSMB design [8,24], which requires an isochronous lattice. A diagram of this lattice is presented in Fig. 1. The phase space of the electron beam is defined as $(x, x', y, y', z, \delta)$. The electrons are modulated at the first laser modulator (LM1) and receive an energy kick as

$$\delta_1 = \delta_0 - V_1/E_0 \sin(k_l z_0), \tag{1}$$

where V_1 represents the equivalent modulation voltage, E_0 denotes the beam energy, $k_l = 2\pi/\lambda_l$ is the wave number of the modulation laser, where λ_l is the laser wavelength. The modulation strength h_1 is defined as $h_1 = V_1 k_l/E_0$.

The electron bunch will then be guided through the chicane with an appropriate momentum compaction R56. With the optimized design, the electron bunch is expected to become microbunched at the radiator, enabling coherent radiation at short wavelengths. To sustain this process at a very high repetition rate, the electron bunch must be recovered in the downstream lattice after the radiator. The simplest approach is to use a lattice with negative momentum compaction, −R56, to first reverse the compression, followed by applying a negative modulation, −LM1, to accomplish the demodulation.

If the lattice between the LM1 and −LM1 is not isochronous, a path length deviation Δz will occur (which is the same as the definition of Δt in Sec. I). This will result

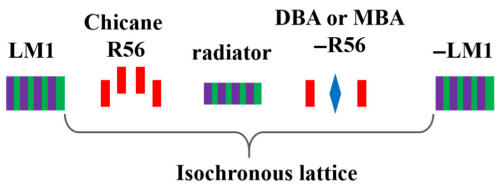


FIG. 1. Sketch of SSMB isochronous lattice.

in an energy kick $\Delta\delta$ being induced throughout the entire lattice given by

$$\begin{aligned}\delta_2 &= \delta_1 + V_1/E_0 \sin(k_l z_0 + k_l \Delta z)\\ &\approx \delta_0 + h_1 \Delta z \cos(k_l z_0)\\ \Delta\delta &= \delta_2 - \delta_0\\ &= h_1 \Delta z \cos(k_l z_0),\end{aligned} \tag{2}$$

here we assume $\Delta z \ll \lambda_l$. Furthermore, assuming that Δz is independent of z_0, the variance of $\Delta\delta$ can be approximately expressed as

$$\mathrm{Var}(\Delta\delta) \approx \frac{1}{2} h_1^2 \mathrm{Var}(\Delta z). \tag{3}$$

Equation (3) shows that the effectiveness of the SSMB scheme is constrained by the isochronous condition of the lattice between the modulation and demodulation stages. This is because any deviation in the electron path length between the two modulators causes a considerable increase in energy spread, which, if not controlled, reduces the radiation power. To attain high radiation power—emitting coherently at a very high repetition rate—at a wavelength of λ_r, the standard deviation of Δz must be maintained as [Eq. (18) in Ref. [8]]

$$\sigma_{\Delta z} \lesssim \frac{\lambda_r}{\pi} \frac{1}{\frac{A_1}{\sigma_\delta}} \sqrt{\frac{4}{N_z}}. \tag{4}$$

Here, N_z represents the number of turns in one longitudinal damping time in the storage ring. $A_1 = h_1/k_l$, σ_δ is equilibrium relative energy spread of the beam. Since the bunching factor for radiation depends on A_1 and σ_δ, the radiation power increases, and the requirement for $\sigma_{\Delta z}$ becomes more stringent. More details can be found in Ref. [8]. For instance, if the radiation wavelength is chosen as $\lambda_r = 13.5$ nm and the goal is to achieve an average radiation power of around 1 kW, then the necessary value for $\sigma_{\Delta z}$ is roughly $\sigma_{\Delta z} \sim 0.1$ nm.

The deviation in path length of electron beam particles between the upstream and downstream laser modulators can be caused by various factors, including the quantum excitation from synchrotron radiation in the radiator, intrabeam scattering effects, and lattice nonlinearity. A detailed rough estimate of these effects is provided in Ref. [8]. For example, considering synchrotron radiation, the induced standard deviation of the path length can be calculated using the formula $\sigma_{\Delta z} = |R_{56}| \sqrt{\langle N \rangle \langle \frac{u^2}{E_0^2} \rangle}$, where R_{56} is the local momentum compaction from the radiator to the downstream laser modulator, N is the number of photons emitted by the radiator per pass, u is the photon energy emitted by the radiator, E_0 is the nominal beam energy, and

$\langle\cdots\rangle$ denotes the average over the radiated photons. Using parameters such as a radiator undulator peak field $B_0 = 0.615$ T, radiator length $L_r = 5.7$ m, $E_0 = 600$ MeV, and $R_{56} = 100$ μm, we find $\sigma_{\Delta z} = 0.0477$ nm. This paper will focus on how to achieve this type of lattice design.

Electron motion in the lattice can be described using two approaches: the Taylor map and Lie algebra. Below, we demonstrate that comparing these methods provides a deeper understanding. Our discussion is confined to a six-dimensional phase space system. The phase space vector is given by $\vec{r} = (x, x', y, y', z, \delta)$, while the canonical coordinates are $(x, x_p, y, y_p, z, \delta)$. These two coordinate sets are related by the expressions $x' = \frac{x_p}{1+\delta}, y' = \frac{y_p}{1+\delta}$.

The transport map for an electron beam in the Taylor map formalism is, for $i = 1\ldots6$

$$r_f(i) = \sum_{k=1}^{6} R_{ik} r_0(k) + \sum_{j=1}^{6}\sum_{k=1}^{6} T_{ijk} r_0(j) r_0(k) + \sum_{j=1}^{6}\sum_{k=1}^{6}\sum_{l=1}^{6} Q_{ijkl} r_0(j) r_0(k) r_0(l)\ldots \quad (5)$$

Here, r_f represents the final phase space coordinate, and r_0 denotes the initial phase space coordinate. The symbols R, T, and Q correspond to the first-, second-, and third-order transport maps of the Taylor map, respectively. Higher-order maps are not included in this description.

Our attention is on the deviation in path length, which can be represented as

$$\Delta z = R_{51} x_0 + R_{52} x_0' + R_{56}\delta + \sum_{i=1}^{6}\sum_{j=1}^{6} T_{5ij} r_0(i) r_0(j) + \sum_{j=1}^{6}\sum_{k=1}^{6}\sum_{l=1}^{6} Q_{5jkl} r_0(j) r_0(k) r_0(l)\ldots. \quad (6)$$

Here, we assume that the lattice contains no vertical bending magnets. In an isochronous lattice, the conditions $R_{51} = 0$, $R_{52} = 0$, and $R_{56} = 0$ must be satisfied. However, the perfect isochronous condition can be disrupted by the lattice's nonlinearities.

For an achromat lattice where $R_{56} = 0$, the Hamiltonian can be expressed as follows:

$$H = \nu_x J_x + \nu_y J_y + \sum_{n\geq 3}\sum_{a+b+c+d+e=n} h_{abcde} h_x^{+a} h_x^{-b} h_y^{+c} h_y^{-d} \delta^e, \quad (7)$$

with

$$h_x^+ = \hat{x} - i\hat{p}_x, \quad h_x^- = \hat{x} + i\hat{p}_x$$
$$h_y^+ = \hat{y} - i\hat{p}_y, \quad h_y^- = \hat{y} + i\hat{p}_y$$
$$\hat{x} = \sqrt{2J_x}\cos(\psi_x), \quad \hat{p}_x = -\sqrt{2J_x}\sin(\psi_x)$$
$$\hat{y} = \sqrt{2J_y}\cos(\psi_y), \quad \hat{p}_y = -\sqrt{2J_y}\sin(\psi_y). \quad (8)$$

Here, ν_x and ν_y represent the unperturbed horizontal and vertical betatron tunes, respectively. The variables $\hat{x}$, $\hat{p}_x$, $\hat{y}$, and $\hat{p}_y$ denote the normalized canonical coordinates. The actions J_x and J_y are defined as $J_x = \epsilon_x/2$ and $J_y = \epsilon_y/2$, where ϵ_x and ϵ_y are the rms horizontal and vertical emittances, respectively. The phases ψ_x and ψ_y correspond to the horizontal and vertical betatron phases of the particle. The index n indicates the nonlinear order in the Hamiltonian; specifically, $n = 3$ corresponds to the second-order Taylor map, also known as the T map. And a, b, c, d, e are all natural numbers.

Based on the Hamilton equations of motion, the deviation in the path length of any particle is expected to be

$$\Delta z = \frac{\partial H}{\partial \delta} = \sum_{n\geq 3}\sum_{a+b+c+d+e=n}^{e\geq 1} e h_{abcde} h_x^{+a} h_x^{-b} h_y^{+c} h_y^{-d} \delta^{e-1}. \quad (9)$$

To address this problem, we first examine the nonlinear effects at the lowest order, $n = 3$. Further details are provided in the Appendix.

Attempting to minimize the standard deviation of the electron beam's path length using Eq. (A6) can be challenging, as it involves reducing many coefficients of the T map that account for dynamics in all three directions. Alternatively, a more physically intuitive approach based on the Hamiltonian, presented in Eq. (A11), was explored. From Eq. (A11), it is evident that if we can make $|h_{20001}|=0$, $|h_{00201}|=0, |h_{10002}|=0$ by special lattice arrangement, then the expression for the path length deviation simplifies to the following three terms:

$$\sigma_{\Delta z}^2 = 4h_{11001}^2\epsilon_{x0}^2 + 4h_{00111}^2\epsilon_{y0}^2 + 2h_{00003}^2\sigma_\delta^4. \quad (10)$$

According to Eq. (A11), the term h_{11001} represents horizontal chromaticity, h_{00111} represents vertical chromaticity, and h_{00003} corresponds to the second-order momentum compaction. Therefore, three families of sextupoles are sufficient to correct these three components.

Fortunately, the HOA scheme provides an elegant solution to cancel the terms h_{20001}, h_{00201}, and h_{10002}. As Bengtsson's study [21] shows, the contributions to the Hamiltonian from magnets can be linearly added at order $n = 3$. The phase dependence of the three terms we are focusing on is given by

$$h_{20001} \sim \exp(i2\mu_x)$$
$$h_{00201} \sim \exp(i2\mu_y)$$
$$h_{10002} \sim \exp(i\mu_x). \tag{11}$$

This implies that the three terms can be eliminated by employing an N-periodic lattice and ensuring each lattice has a specific phase advance of $\mu_{x,y} = \frac{k}{N}2\pi$, where k and N are integers and $\frac{k}{N}$ is not integer or half-integer. Therefore, the smallest possible value for N is 3.

Although all terms related to path length deviation at order $n = 3$ can be completely canceled and corrected using sextupoles, the higher-order terms at $n = 4$ generated by these sextupoles cannot be eliminated, according to Wang's study [25]. For the Hamiltonian at order $n = 4$, there are numerous terms associated with path length deviation. Similar to the approach taken for $n = 3$, we can compute the standard deviation of the path length for order $n = 4$. The results are presented in Eq. (A13) in the Appendix. The problem is transferred to minimize the path length deviation arising from the fourth-order terms in the HOA lattice, when sextupoles are employed to correct chromaticities and the second-order momentum compaction factor.

III. LATTICE OPTIMIZATION

As mentioned earlier, an isochronous lattice is required for numerous applications. We propose in Sec. II that the HOA lattice can satisfy these stringent requirements of $\sigma_{\Delta z} < 0.3$ nm even when nonlinear dynamics are considered. Here, we use a periodic lattice composed of three identical cells as an example, illustrated in Fig. 2. The lattice selected for each identical cell is depicted in Fig. 3.

We design the identical cell with the linear constraints of

$$\mu_{x,y} = \frac{p * 2\pi}{3}$$
$$R_{56} = 0, \quad R_{51} = 0, \quad R_{52} = 0, \tag{12}$$

where p is any natural integer not divisible by 3, R_{ij} denotes the element in the ith row and jth column of the lattice's linear transfer matrix. Within the lattice, the first four dipoles (B0 and −B0) constitute a chicane that provides a specific momentum compaction for dynamic control. To satisfy the linear constraints, we employ four

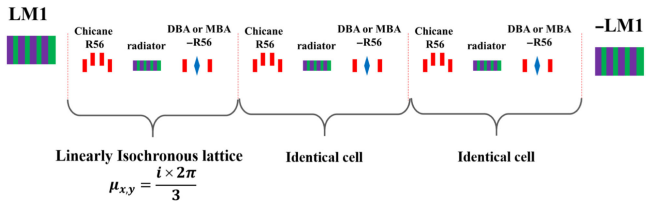


FIG. 2. Sketch of three identical isochronous lattices.

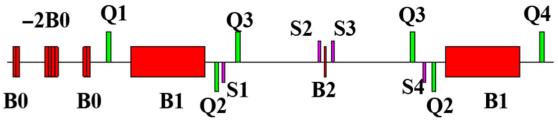


FIG. 3. Lattice chosen for each identical cell. The red rectangles represent dipoles, green rectangles represent quadrupoles, and purple rectangles represent sextupoles. For simplification, the radiator in Fig. 2 is replaced by a drift in the following design example.

families of quadrupoles (Q1 through Q4) and two families of dipoles (B1 and B2), where combined-function dipoles are used.

For nonlinear optimization, we use four families of sextupoles (S1–S4) to provide greater flexibility in minimizing higher-order nonlinearities ($n = 4$). The nonlinear constraints require that the chromaticities (h_{11001} and h_{00111}) and the second-order momentum compaction (h_{00003}) be zero within the identical cell. We do not use octupoles in the optimization, which can be added when needed. The optimization goal is to minimize the standard deviation of the path length, as shown in Eq. (A13). The coefficients h_{abcde} at order $n = 4$ are calculated following Wang's method [25].

In the end, we obtain the optimal solution with a path length standard deviation of approximately $\sigma_{\Delta z} \approx 0.1$ nm. The beam emittance values are $\epsilon_x = 1$ nm, $\epsilon_y = 1$ nm, and the energy spread is $\sigma_\delta = 1 \times 10^{-3}$. Figure 4 displays the

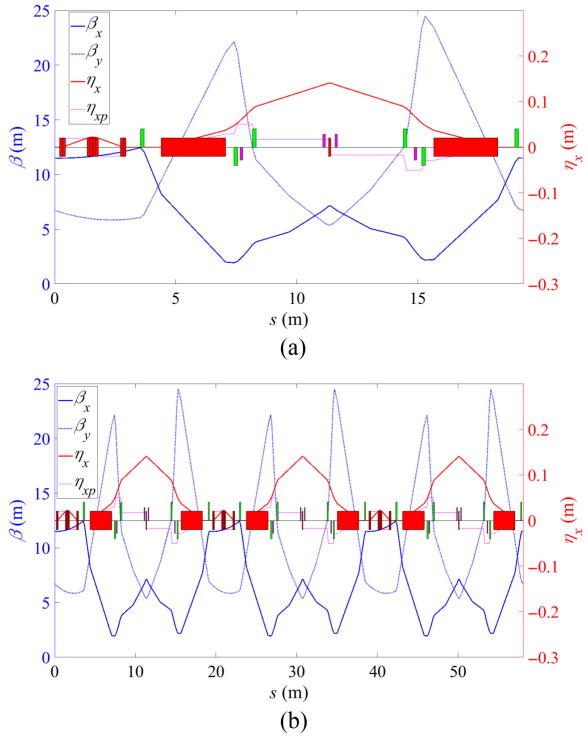


FIG. 4. Twiss functions for each identical cell (a) and total lattice (b).

TABLE I. Strengths of sextupoles and the T-matrix coefficients of the total lattice.

Parameters	Value
Sextupoles strength [K2]	$-92.7/58.1/58.6/-72.5$
T_{511}	-1.1×10^{-4}
T_{512}	-4.6×10^{-4}
T_{522}	1.4×10^{-2}
T_{533}	-1.7×10^{-7}
T_{534}	-4.9×10^{-7}
T_{544}	2.6×10^{-6}
T_{561}	6.6×10^{-6}
T_{562}	1.7×10^{-5}
T_{566}	-2.8×10^{-10}

TABLE II. Hamiltonian coefficients related to path length at order $n=4$ after optimization.

Parameters	Value
h_{00004}	-0.0163
h_{10003}	$-0.0068-0.0017i$
h_{11002}	5.157
h_{00112}	-3.168
h_{20002}	$-0.724-0.148i$
h_{00202}	$-1.144-0.847i$
h_{30001}	$158.92-230.36i$
h_{21001}	$-55.19-19.82i$
h_{10201}	$62.88+66.31i$
h_{10111}	$37.54+59.92i$
h_{10021}	$273.96+576.14i$

Twiss parameters for each identical cell as well as for the entire lattice.

In our optimization, the electron beam energy is fixed at 900 MeV, and the chicane's R_{56} is 800 μm. The strengths of the sextupoles and the elements T_{5ij} for the fully optimized lattice are presented in Table I. It is evident that the contribution to the path length from the third order ($n=3$) has been effectively canceled by the HOA lattice design.

It is important to mention that we have also thoroughly optimized the contribution from higher-order terms $n=4$ using Eq. (A13), without invoking octupoles. The optimized coefficients of h_{abced} that we are interested in are presented in Table II. Using the data from Table II, the path length deviation can be computed as $\sigma_{\Delta z}=0.095$ nm according to Eq. (A13).

TABLE III. Beam parameters for ELEGANT tracking simulation.

Parameters	Value
Horizontal emittance	1 nm
Vertical emittance	1 nm
Energy spread	1×10^{-3}
Bunch length	1 mm
Macroparticle number	10,000

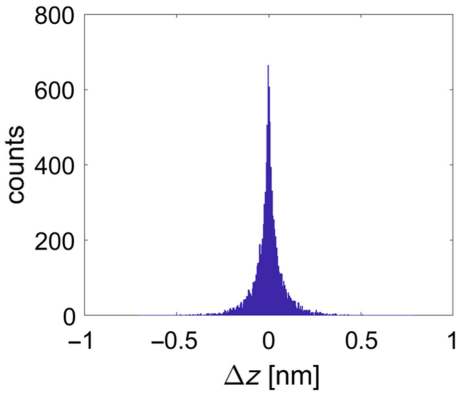


FIG. 5. Histogram of Δz.

Next, we utilize ELEGANT tracking [26] to verify that our design meets the specified requirements. This tracking simulation is conducted in a single passage through the three-cell lattice. The initial beam parameters are provided in Table III.

We placed the observation points at the lattice's entrance and exit. The value of Δz is determined by the difference between the exit coordinate z_f and the entrance coordinate z_i, expressed as $\Delta z=z_f-z_i$. The histogram of Δz is shown in Fig. 5. The standard deviation of Δz was computed from the data, yielding $\sigma_{\Delta z}=0.091$ nm, which corresponds to 0.3 attoseconds. This result meets our requirements very well. Additionally, we observed that the simulation results closely match our analytical calculation given in Eq. (A13).

IV. PRELIMINARY STUDY ON MISALIGNMENT ERROR OF QUADRUPOLES

To gain some understanding of error tolerance, we conduct an initial study by introducing misalignment errors to the quadrupoles in the lattice, as shown in Fig. 4. The beam parameters are the same as in Table III.

First, we introduce four groups of errors with varying misalignments of $2,4,20,40$ μm in both horizontal and vertical directions for all quadrupoles. These errors are random and follow a Gaussian distribution. In ELEGANT, the random sequences are created using different random seeds. We compute the standard deviation $\sigma_{\Delta z}$ and the

TABLE IV. Path length deviation for different errors.

Misalignment error (μm)	$\sigma_{\Delta z}$ (nm)	$\langle\Delta z\rangle$ (μm)
2	0.484	0.244
4	0.973	0.485
20	4.874	2.414
40	9.652	4.823

TABLE V. Path length deviation for different random seeds. The misalignment error of quadrupoles is 2 μm.

Seed number	$\sigma_{\Delta z}$ (nm)	$\langle \Delta z \rangle$ (μm)
1	0.484	0.244
2	0.723	−0.107
3	0.690	−0.0213
4	0.609	0.0744
5	0.595	0.0313

mean value $\langle \Delta z \rangle$ of the path length deviation for the four error groups, with the results presented in Table IV.

We also perform tracking using various random seeds for a specific misalignment error of 2 μm. The results are shown in Table V.

The average path length deviation of the bunch, shown in Tables IV and V, is no longer zero but changes significantly when misalignment errors are introduced. This is because electrons experience an equivalent dipole magnetic field when the quadrupoles are misaligned.

The results shown in Table IV also demonstrate a strong linear correlation between the deviation in path length and the misalignment error. This linear relationship suggests that the primary effects may arise from the linear matrix mismatch caused by these errors. Error corrections are necessary because $\sigma_{\Delta z}$ is at the 10 nm level despite a misalignment error of 40 μm. We will provide an initial analysis of the main targets to be corrected, but the actual correction process will be addressed in a future study.

As mentioned earlier, the increase in path length deviation caused by misalignment errors primarily results from mismatches in the linear matrix. The relevant matrix elements involved are $R_{51}, R_{52}, R_{53}, R_{54}$, and R_{56}, which should be zero without error in our isochronous lattice. We will examine each of these elements individually.

We first address the horizontal dimension, omitting the vertical dimension since it behaves similarly to the horizontal direction. Using the notation from Eq. (A2), the path length deviation arising from the horizontal direction is given by

$$\begin{aligned}\Delta z &= R_{51}x + R_{52}x' \\ &= \sqrt{2J_x}\left[\frac{R_{51}\beta_x - \alpha_x R_{52}}{\sqrt{\beta_x}}\cos(\psi_x) - \frac{R_{52}}{\sqrt{\beta_x}}\sin(\psi_x)\right] \\ &= \sqrt{2J_x H_x}\cos(\psi_x + \phi_0), \end{aligned} \tag{13}$$

with

$$\begin{aligned} H_x &= \beta_x R_{51}^2 - 2\alpha_x R_{51}R_{52} + \gamma_x R_{52}^2 \\ \tan\phi_0 &= \frac{R_{52}}{\beta_x R_{51} - \alpha_x R_{52}}. \end{aligned} \tag{14}$$

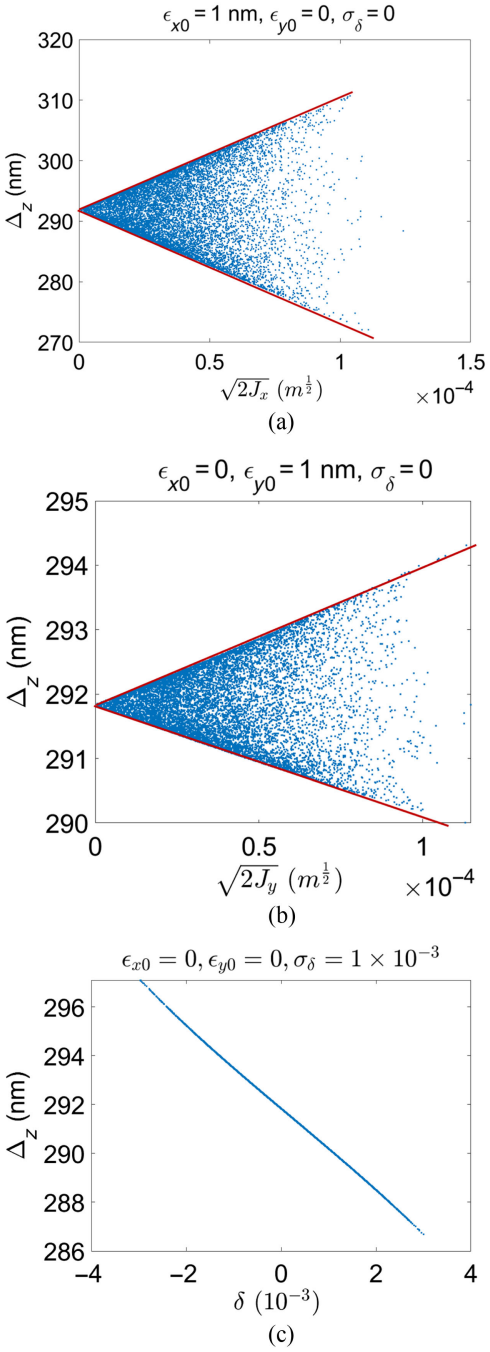


FIG. 6. Path length deviation for different sets of beam parameters. The misalignment error for all quadrupoles is 20 μm. (a) Path length deviation vs particle horizontal betatron amplitude. (b) Path length deviation vs particle vertical betatron amplitude. (c) Path length deviation vs particle energy spread.

The nonzero elements R_{51} and R_{52} arise due to misalignment errors, and ψ_x represents the betatron phase of the particle at the lattice entrance. It is evident that the deviation in path length is directly proportional to R_{51} and R_{52}, and therefore, it is linearly related to the misalignment error.

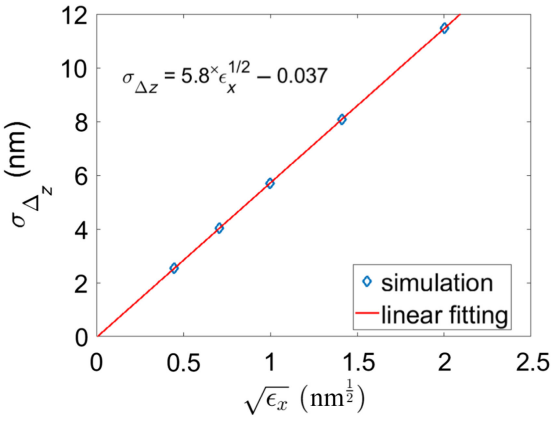


FIG. 7. Relation of $\sigma_{\Delta z}$ and horizontal beam rms emittance when 20 μm misalignment error of quadrupoles is introduced.

Additionally, we can determine the standard deviation of Δz in Eq. (13) by taking the average over the beam distribution. The result will be

$$\sigma_{\Delta z} = \sqrt{H_x \epsilon_x}, \tag{15}$$

with ϵ_x is the rms horizontal emittance of the beam.

Concerning the longitudinal dimension, there is a distinct linear correlation expressed as $\Delta z = R_{56}\delta$.

The average path length deviation can be corrected by tuning the laser phase of the downstream laser modulator in SSMB scenarios. Therefore, in the following simulations, we primarily focus on the standard deviation $\sigma_{\Delta z}$.

We confirm the analysis by running simulations that include a 20 μm misalignment error in the quadrupoles along both the horizontal and vertical axes. To study each direction separately, we categorize the beam parameters into three groups as $(\epsilon_{x0} = 1\,\text{nm}, \epsilon_{y0} = 0, \sigma_\delta = 0)$, $(\epsilon_{x0} = 0, \epsilon_{y0} = 1\,\text{nm}, \sigma_\delta = 0)$, and $(\epsilon_{x0} = 0, \epsilon_{y0} = 0, \sigma_\delta = 1 \times 10^{-3})$. The simulations are performed by ELEGANT. The results are shown in Fig. 6.

In Fig. 6(c), the linear relationship is clearly evident. In Figs. 6(a) and 6(b), the linear relationship is confirmed by the red boundary we marked in the figures. The particles within this boundary represent different betatron phases at the lattice entrance.

We also perform another simulation by varying the horizontal beam emittance, keeping $\epsilon_y = 0$ and $\sigma_\delta = 0$. A misalignment error of 20 μm is applied to all quadrupoles in both horizontal and vertical directions, while the random seed remains constant as the horizontal emittance changes. The standard deviation $\sigma_{\Delta z}$ is calculated from the data and presented in Fig. 7. The results shown in Fig. 7 confirm the conclusion given in Eq. (15). Based on the fitting, we estimate that the variation in H_x along the lattice transport line caused by the 20 μm quadrupole misalignment error is approximately $\sqrt{H_x} = 5.8\ \text{nm}^{1/2}$.

We then do a simple summary for the discussions in this section. The main focus for correcting errors caused by quadrupole misalignment should be the linear matrix. According to the notation used in this paper, the correction targets are the changes in the horizontal function H_x, the vertical function H_y, and R_{56} along the lattice transport line. To maintain the isochronous condition within 0.1 nm, the limits for linear map correction are approximately $H_x \sim 10$ pm (which corresponds to a change in horizontal dispersion $\Delta\eta_x \sim 10$ μm if $\beta_x = 10$ m), $H_y \sim 10$ pm (corresponding to $\Delta\eta_y \sim 10$ μm if $\beta_y = 10$ m), and $\Delta R_{56} \sim 0.1$ μm. These limits apply for beam parameters of $\epsilon_x = 1$ nm, $\epsilon_y = 1$ nm, and $\sigma_\delta = 1 \times 10^{-3}$.

V. SUMMARY

In this study, we propose that an isochronous lattice incorporating nonlinear dynamics can be realized through the HOA lattice design approach. We provide a theoretical analysis up to the third order ($n = 3$) and explain why the HOA lattice satisfies the isochronous condition at this order. Additionally, we offer an estimation of the path length deviation at the fourth order ($n = 4$) and use this as the basis for optimization. As an example, we design an appropriate lattice using three periodic cells and identify a solution that fulfills our criteria. We then perform macroparticle tracking simulations with ELEGANT to validate our results, achieving a path length deviation of $\sigma_{\Delta z} = 0.091$ nm (time-of-flight fluctuation is about 0.3 attoseconds) at beam emittances of $\epsilon_x = 1$ nm, $\epsilon_y = 1$ nm, and an energy spread $\sigma_\delta = 1 \times 10^{-3}$. We also conduct an initial investigation into how quadrupole misalignment errors affect the isochronous condition. The initial conclusion is that the primary problem is the linear matrix mismatch, and a rough estimate of the error correction criterion is provided.

ACKNOWLEDGMENTS

This work is supported by the National Key R&D Program of China (Grant No. 2022YFA1603402) and Beijing Natural Science Foundation (Grant No. 1254058), the National Natural Science Foundation of China (NSFC Grant No. 12035010), and the Tsinghua University Initiative Scientific Research Program.

DATA AVAILABILITY

The data that support the findings of this article are not publicly available. The data are available from the authors upon reasonable request.

APPENDIX: COMPARISON FOR TAYLOR MAP AND LIE ALGEBRA

1. Nonlinearities up to order $n = 3$

In Taylor map formalism, the path length deviation for a linearly isochronous lattice (where the lattice is achromatic

and $R_{56} = 0$) is represented as follows:

$$\Delta z = T_{511}x^2 + 2T_{512}xx' + T_{522}x'^2 + T_{533}y^2 + 2T_{534}yy' + T_{544}y'^2 + 2T_{561}x\delta + 2T_{562}x'\delta + T_{566}\delta^2. \tag{A1}$$

Here, we assume that there is no coupling between the horizontal and vertical directions, and that all bending magnets are oriented horizontally. Our discussion is confined to the T map. Higher-order Taylor terms are omitted. The betatron motion can be expressed as follows:

$$\begin{aligned} x &= \sqrt{2\beta_x J_x}\cos(\psi_x) \\ x' &= -\sqrt{\frac{2J_x}{\beta_x}}\sin(\psi_x) - \alpha_x\sqrt{\frac{2J_x}{\beta_x}}\cos(\psi_x) \\ y &= \sqrt{2\beta_y J_y}\cos(\psi_y) \\ y' &= -\sqrt{\frac{2J_y}{\beta_y}}\sin(\psi_y) - \alpha_y\sqrt{\frac{2J_y}{\beta_y}}\cos(\psi_y). \end{aligned} \tag{A2}$$

Here, $\alpha_x, \beta_x, \alpha_y, \beta_y$ represent the Twiss parameters in the horizontal and vertical planes, while ψ_x and ψ_y denote the betatron phase of the electron in the horizontal and vertical directions, respectively.

Inserting Eq. (A2) into Eq. (A1), one can get

$$\begin{aligned} \Delta z = {} & \Omega_{x1}J_x + \left(\Omega_{x1} - \frac{2}{\beta_x}T_{522}\right)J_x\cos(2\psi_x) + \left(\frac{\alpha_x T_{522}}{\beta_x} - T_{512}\right)2J_x\sin(2\psi_x) + \Omega_{y1}J_y \\ & + \left(\Omega_{y1} - \frac{2}{\beta_y}T_{544}\right)J_y\cos(2\psi_y) + \left(\frac{\alpha_y T_{544}}{\beta_x} - T_{534}\right)2J_y\sin(2\psi_y) \\ & + 2T_{561}\sqrt{2\beta_x J_x}\cos(\psi_x)\delta - 2T_{562}\sqrt{\frac{2J_x}{\beta_x}}\sin(\psi_x)\delta - 2T_{562}\alpha_x\sqrt{\frac{2J_x}{\beta_x}}\cos(\psi_x)\delta + T_{566}\delta^2, \end{aligned} \tag{A3}$$

with

$$\begin{aligned} \Omega_{x1} &= \beta_x T_{511} - 2\alpha_x T_{512} + \gamma_x T_{522} \\ \Omega_{y1} &= \beta_y T_{533} - 2\alpha_y T_{534} + \gamma_y T_{544}, \end{aligned} \tag{A4}$$

while $\gamma_x\beta_x = 1 + \alpha_x^2$, $\gamma_y\beta_y = 1 + \alpha_y^2$. We define the average bracket as $\langle f_0 \rangle$,

$$\langle f_0 \rangle = \int_0^\infty d\epsilon_x \int_0^\infty d\epsilon_y \int_{-\infty}^\infty \mathrm{d}\delta \int_0^{2\pi} d\psi_x \int_0^{2\pi} d\psi_y f_0 \Psi(\epsilon_x)\Psi(\epsilon_y)\Psi(\delta), \tag{A5}$$

with $\Psi(\epsilon_x) = \frac{1}{2\epsilon_{x0}}\exp(-\frac{\epsilon_x}{2\epsilon_{x0}})$, $\Psi(\epsilon_y) = \frac{1}{2\epsilon_{y0}}\exp(-\frac{\epsilon_y}{2\epsilon_{y0}})$, $\Psi(\delta) = \frac{1}{\sqrt{2\pi}\sigma_\delta}\exp(-\frac{\delta^2}{2\sigma_\delta^2})$. ϵ_{x0} is root mean square (rms) horizontal emittance of the electron bunch, ϵ_{y0} is rms vertical emittance of the electron bunch, and σ_δ denotes energy spread of the electron bunch.

Then one can get [27]

$$\begin{aligned} \langle \Delta z \rangle &= \Omega_{x1}\epsilon_{x0} + \Omega_{y1}\epsilon_{y0} + T_{566}\sigma_\delta^2 \\ \sigma_{\Delta z}^2 &= \langle \Delta z^2 \rangle - \langle \Delta z \rangle^2 \\ &= \Sigma_{x1}\epsilon_{x0}^2 + \Sigma_{y1}\epsilon_{y0}^2 + \Sigma_2\epsilon_{x0}\sigma_\delta^2 + 2T_{566}^2\sigma_\delta^4 \end{aligned}$$

with

$$\begin{aligned} \Sigma_{x1} &= 2\Omega_{x1}^2 + 4(T_{512}^2 - T_{511}T_{522}) \\ \Sigma_{y1} &= 2\Omega_{y1}^2 + 4(T_{534}^2 - T_{533}T_{544}) \\ \Sigma_2 &= 4T_{561}^2\beta_x - 8T_{561}T_{562}\alpha_x + 4T_{562}^2\gamma_x. \end{aligned} \tag{A6}$$

Given the electron beam emittance, it is necessary to minimize the four terms Σ_{x1}, Σ_{y1}, Σ_2, and T_{566} simultaneously in order to keep $\sigma_{\Delta z}^2$ very small.

The Taylor map provides an effective method to optimize the nonlinear effects of the lattice when the transfer maps R and T are available. Including the Q map would make the process extremely complex [Q is the higher-order Taylor map in Eq. (5)]. Even without the Q map, optimizing the problem, as illustrated in Eq. (A6), remains challenging. In theory, the issue could be addressed by employing more than five families of sextupoles to correct the T map; however, this approach might result in a significantly large $\sigma_{\Delta z}^2$ arising from the Q map.

Next, we encounter the same issue using Lie algebra. For an achromat lattice where $R_{56} = 0$, the system's Hamiltonian can be expressed as follows:

$$z = \exp(-: H :)z_0$$

$$H = \nu_x J_x + \nu_y J_y + \frac{1}{2}h_{20001}h_x^{+2}\delta + \frac{1}{2}h_{02001}h_x^{-2}\delta + h_{11001}h_x^{+}h_x^{-}\delta + \frac{1}{2}h_{00201}h_y^{+2}\delta + \frac{1}{2}h_{00021}h_y^{-2}\delta + h_{00111}h_y^{+}h_y^{-}\delta + \frac{1}{4}h_{10002}h_x^{+}\delta^2 + \frac{1}{4}h_{01002}h_x^{-}\delta^2 + \frac{1}{3}h_{00003}\delta^3 \tag{A7}$$

h_{20001} and h_{02001} are mutually conjugate complex numbers. Similarly, h_{00201} and h_{00021}, as well as h_{10002} and h_{01002}, are mutually conjugate. We define

$$\begin{aligned} h_{20001} &= K_{rx} + iK_{ix} \\ h_{00201} &= K_{ry} + iK_{iy} \\ h_{10002} &= K_{rd} + iK_{id}. \end{aligned} \tag{A8}$$

Using the Hamilton equation of motion $\Delta z = \frac{\partial H}{\partial \delta}$, one can get

$$\begin{aligned} \Delta z = {} & h_{11001}2J_x + h_{00111}2J_y + (K_{rx}\cos(2\psi_x) - K_{ix}\sin(2\psi_x))2J_x + (K_{ry}\cos(2\psi_y) - K_{iy}\sin(2\psi_y))2J_y \\ & + (K_{rd}\cos(\psi_x) - K_{id}\sin(\psi_x))\sqrt{2J_x}\delta + h_{00003}\delta^2. \end{aligned} \tag{A9}$$

Comparing Eq. (A9) to Eq. (A3), the relationship between the Hamiltonian parameters and the Taylor map parameters can be expressed as follows.

$$\begin{aligned} h_{11001} &= \Omega_{x1}/2, \quad h_{00111} = \Omega_{y1}/2, \\ 2K_{rx} &= \Omega_{x1} - \frac{2}{\beta_x}T_{522}, \quad K_{ix} = T_{512} - \frac{\alpha_x T_{522}}{\beta_x}, \\ 2K_{ry} &= \Omega_{y1} - \frac{2}{\beta_y}T_{544}, \quad K_{iy} = T_{534} - \frac{\alpha_y T_{544}}{\beta_y}, \\ K_{rd} &= 2T_{561}\sqrt{\beta_x} - 2T_{562}\frac{\alpha_x}{\sqrt{\beta_x}}, \quad K_{id} = \frac{2T_{562}}{\sqrt{\beta_x}}, \\ h_{00003} &= T_{566}. \end{aligned} \tag{A10}$$

We can also calculate the average value and variance of Δz from Eq. (A9), the result is shown below

$$\begin{aligned} \langle \Delta z \rangle &= 2h_{11001}\epsilon_{x0} + 2h_{00111}\epsilon_{y0} + h_{00003}\sigma_\delta^2 \\ \sigma_{\Delta z}^2 &= 4h_{11001}^2\epsilon_{x0}^2 + 4|h_{20001}|^2\epsilon_{x0}^2 + 4h_{00111}^2\epsilon_{y0}^2 + 4|h_{00201}|^2\epsilon_{y0}^2 + |h_{10002}|^2\epsilon_{x0}\sigma_\delta^2 + 2h_{00003}^2\sigma_\delta^4. \end{aligned} \tag{A11}$$

Substituting Eq. (A10) into Eq. (A6) yields the same results as those in Eq. (A11).

2. Nonlinearities up to order $n = 4$

For the case of order $n = 4$, we focus solely on our problem within the Lie algebra framework. Analogous to Eq. (A9), the path length deviation for order $n = 4$ can be expressed as follows.

$$\begin{aligned}\Delta z = {} & h_{21001}h_x^{+2}h_x^- + h_{30001}h_x^{+3} + h_{10201}h_x^+h_y^{+2} + h_{10111}h_x^+h_y^+h_y^- + h_{10021}h_x^+h_y^{-2} + h_{11002}h_x^+h_x^-\delta + h_{00112}h_y^+h_y^-\delta \\ & + h_{20002}h_x^{+2}\delta + h_{00202}h_y^{+2}\delta + h_{10003}h_x^+\delta^2 + h_{00004}\delta^3 + c.c., \end{aligned} \tag{A12}$$

we then compute the mean and variance of Δz, with the results shown below.

$$\begin{aligned}\langle \Delta z\rangle &= 0 \\ \sigma_{\Delta z}^2 &= 15h_{00004}^2\sigma_\delta^6 + 6|h_{10003}|^2\epsilon_{x0}\sigma_\delta^4 + 12h_{00004}(h_{11002}\epsilon_{x0} + h_{00112}\epsilon_{y0})\sigma_\delta^4 + 8Re(h_{10003}h_{21001}^\star)\epsilon_{x0}^2\sigma_\delta^2 \\ &\quad + 4Re(h_{10003}h_{10111}^\star)\epsilon_{x0}\epsilon_{y0}\sigma_\delta^2 + (8h_{11002}^2 + 4|h_{20002}|^2)\epsilon_{x0}^2\sigma_\delta^2 + (8h_{00112}^2 + 4|h_{00202}|^2)\epsilon_{y0}^2\sigma_\delta^2 \\ &\quad + 8h_{11002}h_{00112}\epsilon_{x0}\epsilon_{y0}\sigma_\delta^2 + 24(|h_{21001}|^2 + |h_{30001}|^2)\epsilon_{x0}^3 + 8|h_{10111}|^2\epsilon_{x0}\epsilon_{y0}^2 + 8|h_{10201}|^2\epsilon_{x0}\epsilon_{y0}^2 \\ &\quad + 8|h_{10021}|^2\epsilon_{x0}\epsilon_{y0}^2 + 16\mathrm{Re}(h_{21001}h_{10111}^\star)\epsilon_{x0}^2\epsilon_{y0}, \end{aligned} \tag{A13}$$

where $\mathrm{Re}(Z)$ means the real part of a complex number Z.

[1] F. Qi, Z. Ma, L. Zhao, Y. Cheng, W. Jiang, C. Lu, T. Jiang, D. Qian, Z. Wang, W. Zhang, P. Zhu, X. Zou, W. Wan, D. Xiang, and J. Zhang, Breaking 50 femtosecond resolution barrier in MeV ultrafast electron diffraction with a double bend achromat compressor, Phys. Rev. Lett. **124**, 134803 (2020).

[2] A. Zholents, L. Rebuffi, and X. Shi, Stochastic cooling of electrons and positrons with EUV light, Phys. Rev. Accel. Beams **24**, 022803 (2021).

[3] J. Jarvis, V. Lebedev, A. Romanov, D. Broemmelsiek, K. Carlson, S. Chattopadhyay, A. Dick, D. Edstrom, I. Lobach, S. Nagaitsev *et al.*, Experimental demonstration of optical stochastic cooling, Nature (London) **608**, 287 (2022).

[4] A. Zholents, Isochronous lattice design study for cooling insertion in the electron storage ring, Technical Report No. LS-376, Argonne National Laboratory, 2024.

[5] D. F. Ratner and A. W. Chao, Steady-state microbunching in a storage ring for generating coherent radiation, Phys. Rev. Lett. **105**, 154801 (2010).

[6] X. Deng, A. Chao, J. Feikes, A. Hoehl, W. Huang, R. Klein, A. Kruschinski, J. Li, A. Matveenko, Y. Petenev *et al.*, Experimental demonstration of the mechanism of steady-state microbunching, Nature (London) **590**, 576 (2021).

[7] A. Kruschinski, X. Deng, J. Feikes, A. Hoehl, R. Klein, J. Li, M. Ries, and A. Chao, Confirming the theoretical foundation of steady-state microbunching, Commun. Phys. **7**, 160 (2024).

[8] X. Deng, Z. Pan, J. Zhao, Z. Li, A. Chao, and C. Tang, Reversible microbunching in an electron storage ring, Phys. Rev. Accel. Beams (to be published).

[9] C. Li, B. Jiang, C. Feng, Q. Gu, Z. Bai, W. Wan, Q. Zhang, and K. Wang, Toward a storage ring coherent light source based on an angular dispersion-induced microbunching scheme, J. Synchrotron Radiat. **32**, 82 (2025).

[10] B. Jiang, C. Feng, C. Li, Z. Bai, W. Wan, D. Xiang, Q. Gu, K. Wang, Q. Zhang, D. Huang *et al.*, A synchrotron-based kilowatt-level radiation source for EUV lithography, Sci. Rep. **12**, 3325 (2022).

[11] W. Liu, Y. Zhao, X. Li, S. Wang, Y. Jiao, and C. Feng, Method for reversing the laser modulation in a storage ring, Phys. Rev. Accel. Beams **28**, 060703 (2025).

[12] Z. Pan. Research on optimization and design of advanced laser-driving storage ring, Ph.D. thesis, Tsinghua University, Beijing, China, 2020.

[13] Z. Pan, A. Chao, X. Deng, W.-H. Huang, T. Rui, C. Tang, W. Wan, and Y. Zhang, A storage ring design for steady-state microbunching to generate coherent EUV light source, in *Proceedings of the 39th Free Electron Laser Conference, Hamburg, Germany* (JACoW, Geneva, Switzerland, 2019), 10.18429/JACoW-FEL2019-THP055.

[14] D. Robin, E. Forest, C. Pellegrini, and A. Amiry, Quasi-isochronous storage rings, Phys. Rev. E **48**, 2149 (1993).

[15] L. Lin and C. E. T. Gonçalves da Silva, Second order single particle dynamics in quasi-isochronous storage rings and its application to the LNLS-UVX ring, Nucl. Instrum. Methods Phys. Res., Sect. A **329**, 9 (1993).

[16] C. Wang and A. Chao, Analytic second-and third-order achromat designs, in *Proceedings Particle Accelerator Conference* (IEEE, New York, 1995), Vol. 5, pp. 2838–2840.

[17] C. Wang and A. Chao, Notes on Lie algebraic analysis of achromats, Technical Report No. SLAC/AP-100, SLAC National Accelerator Laboratory, Menlo Park, CA, 1995.

[18] W. Wan and M. Berz, Analytical theory of arbitrary-order achromats, Phys. Rev. E **54**, 2870 (1996).

[19] R. Nagaoka, A. Loulergue, A. Bence, P. Brunelle, A. Gamelin, L. Hoummi, A. Nadji, L. Nadolski, M. Tordeux, and A. Vivoli, Study of higher-order achromat lattice as an alternative option for the SOLEIL storage ring upgrade, in *Proceedings of the 10th International Particle Accelerator Conference, Melbourne, Australia* (JACoW, Geneva, Switzerland, 2019), 10.18429/JACoW-IPAC2019-MOPRB005.

[20] W. Wan, Theory and applications of arbitrary-order achromats, Ph.D. thesis, Michigan State University, 1995.

[21] J. Bengtsson, The sextupole scheme for the Swiss Light Source SLS: An analytic approach, Technical Report No. SLS Note 9/97, Paul Scherrer Institute, 1997.

[22] H. Ghasem, N. B. Kraljevic, B. Singh, and I. P. S. Martin, Lattice design for the Diamond-II light source storage ring, Phys. Rev. Accel. Beams **27**, 110704 (2024).

[23] Y. Cai, K. Bane, R. Hettel, Y. Nosochkov, M.-H. Wang, and M. Borland, Ultimate storage ring based on fourth-order geometric achromats, Phys. Rev. Accel. Beams **15**, 054002 (2012).

[24] Z. Li, X. Deng, Z. Pan, C. Tang, and A. Chao, Generalized longitudinal strong focusing in a steady-state microbunching storage ring, Phys. Rev. Accel. Beams **26**, 110701 (2023).

[25] C. Wang, Explicit formulas for 2nd-order driving terms due to sextupoles and chromatic effects of quadrupoles, Technical Report No. ANL/APS/LS-330, Argonne National Laboratory, Argonne, IL, 2012.

[26] M. Borland, ELEGANT: A flexible SDDS-compliant code for accelerator simulation, Technical Report No. ANL/APS/LS-287, Argonne National Laboratory, Argonne, IL, 2000.

[27] Z. Li, Z. Pan, J. Tang, C. Tang, X. Deng, and A. Chao, Analysis of nonlinear deviation in a generalized longitudinal strong focusing unit, in *Proceedings of the International Particle Accelerator Conference (IPAC'24), Nashville, TN* (2024), pp. 751–754, 10.18429/JACoW-IPAC2024-MOPS20.